https://doi.org/10.15407/ujpe69.12.936

V.V. ROMAKA,[1] V.A. ROMAKA,[2] YU.V. STADNYK,[3] L.P. ROMAKA,[3] A.M. HORYN,[3] P.YU. DEMCHENKO,[3] V.Z. PASHKEVYCH[2]

[1] Leibniz Institute for Solid State and Materials Research Dresden (IFW Dresden)
(Helmholtzstraße 20, 01069 Dresden, Germany; e-mail: v.romaka@ifw-dresden.de)
[2] Lviv Polytechnic National University
(12, S. Bandera Str., Lviv 79013, Ukraine)
[3] Ivan Franko National University of Lviv
(6, Kyryla and Mefodiya Str., Lviv 79005, Ukraine)

ELECTRICAL CONDUCTIVITY MECHANISMS OF THE $Tm_{1-x}V_xNiSb$ SEMICONDUCTOR

The structural, thermodynamic, kinetic, and energy characteristics of the $Tm_{1-x}V_xNiSb$ semiconductor are studied over $T = 80$–400 K and $0 \le x \le 0.10$. The present study demonstrates that the crystal structure of TmNiSb is disordered and contains up to 2% of vacancies at the 4a crystallographic site (Tm atoms), which are gradually filled with V atoms up to $x = 0.03$ with further V for Tm substitution. The formation of two types of acceptor states with different depths of occurrence is experimentally determined: small acceptors generated by vacancies in the p-TmNiSb structure, and deep ones presumably formed by the vacancies at the Ni 4c site and correspond to the homogeneity region $Tm_xNi_{1-x}Sb$ typical of other RNiSb half-Heusler phases. The results of the DFT modeling, including ground-state energy, distribution of the density of electronic states (DOS), and the band structure of $Tm_{1-x}V_xNiSb$, are consistent with experimental studies.

Keywords: half-Heusler phases, Fermi level, electronic structure, electrical resistivity, thermopower coefficient.

1. Introduction

Half-Heusler phases are a promising class of thermoelectric materials with high efficiency in converting the thermal energy into electricity [1–4]. A special place is held by the equiatomic RNiSb intermetallics [5] that, depending on the rare earth, crystallize with different structure types. Antimonides RNiSb with R = Ce, Pr, Nd, and Sm crystallize with AlB_2 or ZrBeSi structure type and are characterized by metallic type of conductivity [5, 6]. The RNiSb compounds with rare earths of the Yttrium subgroup crystallize in cubic MgAgAs-type (space group F-43m) [5]. As the most representative of the half-Heusler series, the RNiSb antimonides (R = Y, Gd-Lu) exhibit semiconducting behavior (narrow gap semiconductors) [6, 7]. They can be the basis for new promising thermoelectric or magnetic materials.

Our study of the {Y, Gd, Tm, Lu-Ni–Sb ternary systems [8, 9] revealed the disorder effects in the crystal structure of half-Heusler RNiSb phases with a deficiency of Ni atoms. These structural defects in the RNiSb semiconductors cause the generation of defects of a donor and/or acceptor nature in the crystal structure, and corresponding energy states appear in

Citation: Romaka V.V., Romaka V.A., Stadnyk Yu.V., Romaka L.P., Horyn A.M., Demchenko P.Yu., Pashkevych V.Z. Electrical conductivity mechanisms of the $Tm_{1-x}V_xNiSb$ semiconductor. *Ukr. J. Phys.* **69**, No. 12, 936 (2024). https://doi.org/10.15407/ujpe69.12.936.

the band gap. It opens a possibility to optimize the values of specific electrical conductivity $\sigma(T)$, thermopower coefficient $\alpha(T)$, and thermal conductivity $\kappa(T)$ to achieve the maximum values of thermoelectric Q-factor $Z(T)$ [1]. Previous studies of related semiconductor materials, in particular, $Lu_{1-x}V_xNiSb$ [10], $Lu_{1-x}Zr_xNiSb$ [11, 12], $Er_{1-x}Zr_xNiSb$ [13], $Lu_{1-x}Sc_xNiSb$ [14], and $Er_{1-x}Sc_xNiSb$ [15], revealed the disorder of the RNiSb crystal structure. The crystal structure model of *p*-LuNiSb has vacancies at the 4*a site* of Lu atoms and 4*c* of Ni atoms, which generate defects of an acceptor nature and corresponding acceptor states in the band gap. Isovalence substitution of Sc atoms for Lu in $Lu_{1-x}Sc_xNiSb$ generates defects of a neutral nature, while Zr for Lu substitution – defects of a donor nature (Zr has more *d*-electrons). In the $Lu_{1-x}V_xNiSb$ solid solution, structural defects of the acceptor and donor nature are generated. Thermodynamic modeling of $Lu_{1-x}V_xNiSb$ [10], $Lu_{1-x}Zr_xNiSb$ [12], and $Lu_{1-x}Sc_xNiSb$ [14] solid solutions revealed that configuration entropy plays a crucial role in their stabilization at high temperatures. Authors in [16] studied the $Tm_{1-x}Sc_xNiSb$ continuous solid solution between TmNiSb and ScNiSb (both of MgAgAs-type). They showed that the changes in the chemical composition significantly reduce the thermal conductivity, which leads to a sizable enhancement of the thermoelectric Q-factor. In this context, studying the effect of doping *p*-TmNiSb with V atoms in the $Tm_{1-x}V_xNiSb$ solid solution seems interesting as it should generate structural defects of the donor nature (V has more *d*-electrons than Tm). The results of the structural, thermodynamic, and transport properties accompanied by the energy characteristics of $Tm_{1-x}V_xNiSb$ ($0 \le x \le 0.10$) allow us to understand the nature of the defects of the parent *p*-TmNiSb and the mechanism of doping, which will make the process of optimizing the characteristics of this and related thermoelectric materials predictable.

2. Experimental

Synthesis of the samples of the $Tm_{1-x}V_xNiSb$ solid solution $0 \le x \le 0.10$ is carried out by direct arc melting of the constituent metals (thulium, purity of 99.9 wt. %, vanadium, purity of 99.9 wt. %, nickel, purity of 99.99 wt. %, antimony, purity of 99.999 wt. %.) in a protected argon atmosphere with non-consumable tungsten electrode on a water-cooled copper hearth with Ti ingot as a getter. Depending on the composition, the 3–5 wt. % excess of Sb was added to compensate for the evaporative losses of antimony during the arc melting. For better homogeneity, the alloys were re-melted twice. After the melting, the overall weight loss of the alloys was generally less than 1 wt. %. The arc-melted ingots were placed in evacuated quartz ampoules, annealed at 1073 K for 700 hours, and finally quenched in cold water without breaking the ampoule.

The powder X-ray diffraction (XRD) method was used for the phase analysis (identification of formed phases, STOE STADI P with CuKa1 radiation and DRON-4.0 with Fe$K\alpha$ radiation). Elemental and phase compositions of the produced samples were examined by Scanning Electron Microscopy (SEM) using a TESKAN VEGA 3 LMU scanning microscope with a Link EDX system operated at 20 kV and 60 mA. The quantitative electron probe microanalysis (EPMA) was carried out using an energy-dispersive X-ray analyzer with pure elements as standards.

The data for the crystal structure refinement were collected at room temperature using STOE STADI P (CuKa1 radiation) powder diffractometer (graphite monochromator). Rietveld refinement was performed using the FullProf Suite program package [17].

For the measurements of transport properties, the samples were prepared in the form of parallelepiped ($\sim 1 \times 1 \times 4$ mm), cut by spark erosion from the polycrystalline samples. The temperature and concentration dependences of the electrical resistivity (ρ) were measured in the temperature range of 80–400 K using a two-probe method, a widely accepted technique in our field. The thermopower coefficient (α) measurements were carried out by a standard differential method using pure copper as a reference material in the same temperature range.

The DFT calculations were carried out with the Vienna Ab initio Simulation Package VASP v.5.4.4 [18] with PAW-type potentials [19]. The Perdew–Burke-Enzerhoff exchange-correlation functional in the generalized gradient approximation (GGA) [20] with an $11 \times 11 \times 11$ Monkhorst–Pack k-point set [21] was used. The plane-wave cut-off was set to 400 eV in all calculations. The supercell approach was used for the crystal structures with mixed occupancies. In this case, the symmetry of the lattice was reduced, and all

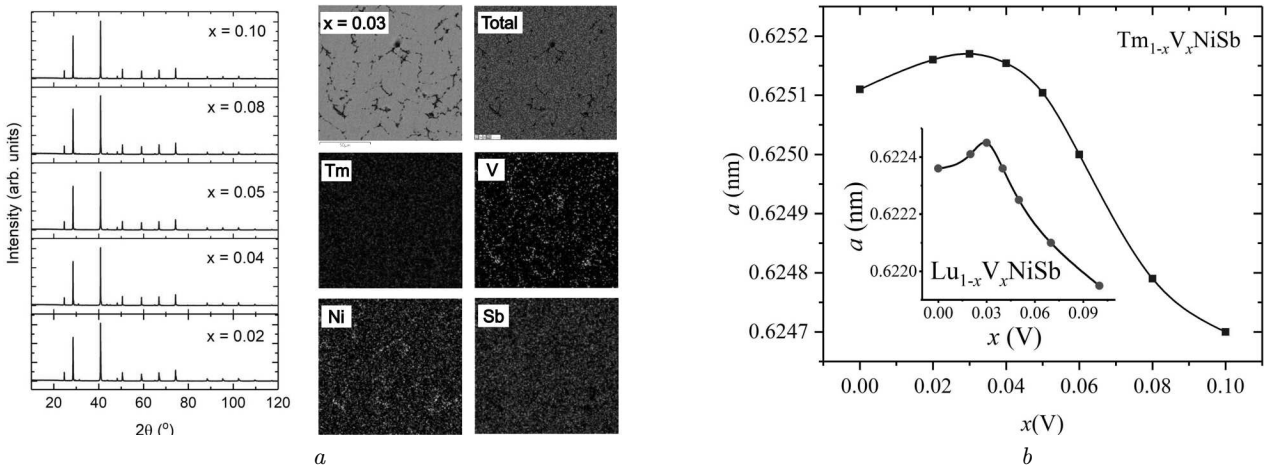

Fig. 1. Experimental XRD powder patterns of the $Tm_{1-x}V_xNiSb$ samples accompanied by the EDX mapping of the $Tm_{0.97}V_{0.03}NiSb$ alloy (a) and the unit cell parameters $a(x)$ of $Tm_{1-x}V_xNiSb$. Inset: $a(x)$ of $Lu_{1-x}V_xNiSb$ [10] (b)

unique atom distributions were generated using the combinatorial approach [22]. The lattice parameters for such structures were optimized by varying lattice volume subsequently fitted by the universal equation of state [23]. Additional calculations were performed using the KKR-CPA method (AkaiKKR code [24]) with local density approximation (LDA) [25] for better convergence to obtain the DOS distribution for low vanadium concentrations.

3. Results and Discussion

3.1. Crystal structure, composition, and thermodynamics

The XRD powder patterns of the annealed samples of the $Tm_{1-x}V_xNiSb$ solid solution ($0 \le x \le 0.1$) were indexed and refined in the MgAgAs structure type (Fig. 1, *a*). On some powder patterns, a broadening of reflections was observed, especially at high diffraction angles 2θ, which may be an indication of the small homogeneity region of the parent TmNiSb phase, which, however, was not observed upon the phase diagram investigation in [9] or the simultaneous presence of doped and undoped crystallites. Further SEM/EDX analysis (Fig. 1, *a*) revealed the presence of trace amounts or precipitates of one of the following phases, depending on the V concentration in the solid solution, which were not detected by powder XRD: Ni_2V (ST $MoPt_2$) or TmSb (ST NaCl). The maximum vanadium solubility obtained by EDX corresponds to the composition $Tm_{0.96(1)}V_{0.04(1)}NiSb$. The lattice parameter a increases with V content up to $x(V) = 0.03$ (Fig. 1, *b*) and gradually decreases for $x(V) > 0.03$, giving a pronounced maximum. Similar behavior was observed in the $Lu_{1-x}V_xNiSb$ [10] (Fig. 1, *b*, insert), $Lu_{1-x}Zr_xNiSb$ [11], and $Er_{1-x}Zr_xNiSb$ [13] solid solutions.

To shed more light on the solubility of V in TmNiSb, we have performed the thermodynamic modeling (PAW method) of the ordered $Tm_{1-x}V_xNiSb$ solid solution for the following concentration of vanadium $x = 0$ (conventional $1 \times 1 \times 1$ cell), 0.03125 ($2 \times 2 \times 2$ supercell), 0.0625 ($2 \times 2 \times 1$ supercell), 0.125 ($2 \times 1 \times 1$ supercell), and hypothetical VNiSb (conventional $1 \times 1 \times 1$ cell). All possible permutations of Tm/V distribution were generated using the combinatorial approach [22]. Manual geometry optimization was performed for all combinations of each concentration by fitting the total energy and lattice volume with the Universal equation of state [23]. The calculated enthalpy of the mixing appeared to be positive for all vanadium concentrations reaching +18.5 meV/atom for $x = 0.0625$, meaning the absence of solubility at low temperatures. However, the introduction of the configurational entropy of the mixing overwhelms the positive enthalpy of the mixing already at 870 K, giving a negative minimum of the Gibbs energy of the mixing ΔG_{mix} (Fig. 2, *a*), which drifts from $x = 0.03$ (870 K) to $x = 0.04$ (1070 K) and reaches $x = 0.05$ (1270 K), which is consistent with experimental results. Despite the calculated concentration dependences of the lat-

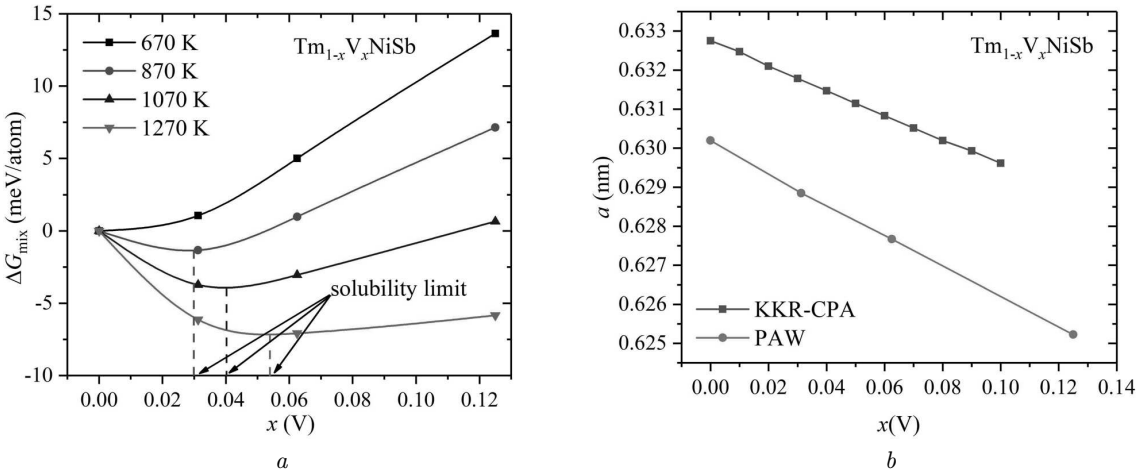

Fig. 2. The calculated Gibbs energy of mixing $\Delta G_{\mathrm{mix}}(x)$ at different temperatures (a) and the modeled by KKR-CPA and PAW methods unit cell parameter $a(x)$ of $Tm_{1-x}V_xNiSb$ (b)

tice parameter using KKR-CPA and PAW methods show descending trends (Fig. 2, b) due to the difference in atomic radii of Tm ($r = 0.174$ nm) and V ($r = 0.134$ nm), they differ from experimental, in particular, in the region $0 \le x \le 0.03$, which indicates a more complex mechanism of doping than the simple V for Tm substitution at the 4a site.

Based on the structural model of disordered LuNiSb [12], the mixture of Tm and vacancies occupies the 4a site, and the mixture of Ni and vacancies occupies the 4c site. We can assume that the increase in unit cell parameter $a(x)$ in the $Tm_{1-x}V_xNiSb$ up to $x = 0.03$ could be caused by simultaneous progressive V for Tm substitution and elimination of vacancies at the 4a site. At higher V content, only V for Tm substitution occurs. The vacancies at the Ni 4c site were observed experimentally in pure YNiSb phase [9] with further confirmation by thermodynamic calculations and did not affect the position of the Fermi level. Instead, they extend the tails of the valence band and decrease the effective energy gap. As the vacancies at the Ni 4c site depend on the composition inside the homogeneity region, we will assume that Ni atoms fully occupy this site to simplify our structural model.

We have used this substitution mechanism to simulate the average atomic radius at the 4a site and the number of electrons per atom (Fig. 3). The simulation shows that at a concentration of ≈ 0.14, the average number of electrons equals 3.0, corresponding to the condition of a fully compensated semiconductor when the Fermi level ε_{F} lies at the middle of the band gap

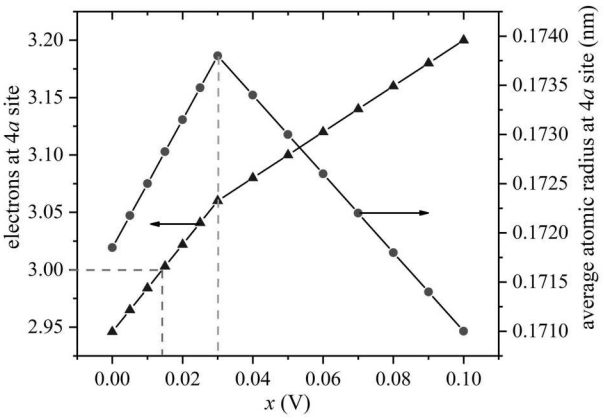

Fig. 3. The effect of simultaneous V for Tm and vacancy substitution at the 4a site of the disordered $Tm_{1-x}V_xNiSb$ structure on the corresponding number of valence electrons per atom and the average atomic radius

ε_g. The average atomic radius increases to $x \approx 0.03$ when all vacancies are filled with V atoms. At higher concentrations, $x > 0.03$, the dependence decreases due to exclusively V for Tm substitution. This result is consistent with the concentration dependence of the lattice parameter a (Fig. 1, b) and qualitatively reproduces its behavior.

3.2. DFT modeling

The DFT modeling was performed for two models of the $Tm_{1-x}V_xNiSb$ solid solution – the ordered one, where Tm atoms at the fully occupied 4a site are

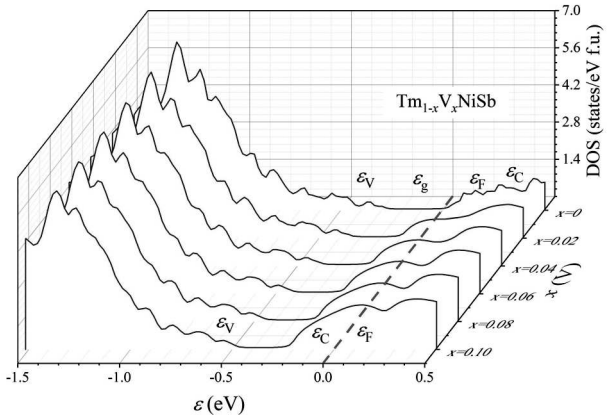

Fig. 4. Distribution of the density of electronic states (DOS) of $Tm_{1-x}V_xNiSb$ (KKR-CPA method) for $0 \le x \le 0.1$. The Fermi level is shifted to 0 eV

substituted solely by V, and the simplified (without accounting vacancies at the 4*c* Ni site) disordered, where V atoms gradually substitute the vacancies and Tm atoms at the 4*a* site.

The distribution of the total electronic density of states in the ordered $Tm_{1-x}V_xNiSb$ (Fig. 4) calculated by the KKR-CPA method shows the Fermi level drifting from the band gap towards the conduction band with the increasing vanadium content. Such substitution generates in $Tm_{1-x}V_xNiSb$ structural defects of the donor nature and the corresponding donor states in the band gap (ε_g), decreasing its effective width.

To have a better look into the contribution of the components of the $Tm_{1-x}V_xNiSb$ solid solution on DOS, we have calculated the total and partial DOS distributions of pure TmNiSb and substituted $Tm_{0.875}V_{0.125}NiSb$ using the PAW method (Fig. 5). The results are consistent with KKR-CPA modeling and show strong impact of the V-states at the Fermi level in the conduction band for the V-doped TmNiSb predicting a change from *p*- to the *n*-type of conductivity. The corresponding band structures of TmNiSb and $Tm_{0.875}V_{0.125}NiSb$ are presented in Fig. 6 and show the Fermi level inside the conduction band for the doped TmNiSb semiconductor. Due to the symmetry reduction upon doping caused by the $2 \times 1 \times 1$ primitive tetragonal supercell, the symmetry points notation differs from those in the fcc TmNiSb.

Using the ordered model of the crystal structure of $Tm_{1-x}V_xNiSb$, one could expect the disappearance of the activation regions on the temperature dependences of electrical resistivity, which will become low and be determined by the scattering of the dominated charge carriers (electrons). As the Fermi level approaches the conduction band and the density of states at the Fermi level increases with V content, the thermopower coefficient should become negative.

The influence of V for Tm substitution on the chemical bonding was evaluated by analyzing the electron localization (ELF) function of $Tm_{0.875}V_{0.125}NiSb$ (Fig. 7) calculated by the PAW method. The isosurface at ELF = 0.375 shows a strong localization between V and Ni atoms, which is absent between Tm and Ni. Nevertheless, a small ELF isosurface could also be spotted around Tm atoms toward four vacant voids at the 4*d* site.

The elastic properties of pure TmNiSb and doped $Tm_{0.875}V_{0.125}NiSb$ were calculated using the PAW method after complete geometry relaxation of both structures. With the introduction of V, the bulk modulus (B) increases from 94.8 to 96.2 GPa, Young's modulus (E) decreases from 148.0 to 141.9 GPa, shear modulus (G) decreases from 59.7 to 56.6 GPa, and the Poisson's ratio (ν) increases from 0.240 to 0.254. The Pugh's B/G ratio for pure (1.59) and substituted (1.70) materials indicates a decrease in the brittle behavior, remaining, however, within the brittle region (< 1.75). It directly reflects the Vickers hardness, which drops from 9.648 to 8.315 GPa for TmNiSb and $Tm_{0.875}V_{0.125}NiSb$, respectively. The calculated Debye temperature slightly decreases from 304.4 to 301.7 K upon doping.

The DFT modeling for the disordered model of the $Tm_{1-x}V_xNiSb$ solid solution was performed using the KKR-CPA method and the approach described in [26]. The distribution of the electronic density of states of $Tm_{0.984}NiSb$ (Fig. 8, *a*) with some vacancies at the 4*a* Tm site shows a formation of acceptor states ε_A, which overlap with the edge of the valence band ε_V, forming the tail of the band (Fig. 8, *a*). Under such circumstances the Fermi level ε_F is located in the tail of the valence band ε_V, and holes becomes the primary charge carriers. The DOS for the disordered $Tm_{0.97}V_{0.018}NiSb$ structure showed that V atoms at the 4*a* site form structural defects of the donor nature, and two types of donor states ε_D appear in the band gap. These states have the highest impact on the total DOS and electrical conductivity of the $Tm_{1-x}V_xNiSb$ semiconductor (Fig. 8, *b*). One could expect the transition from the *p*- to the *n*-type

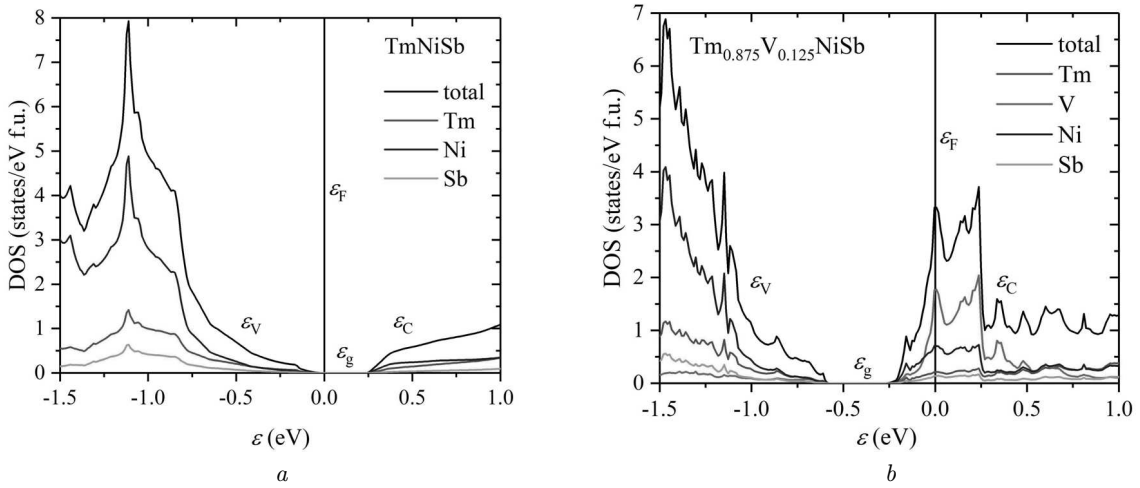

Fig. 5. Distribution of the density of electronic states (DOS) of ordered TmNiSb (*a*) and $Tm_{0.875}V_{0.125}NiSb$ (*b*) (PAW method). The Fermi level is shifted to 0 eV

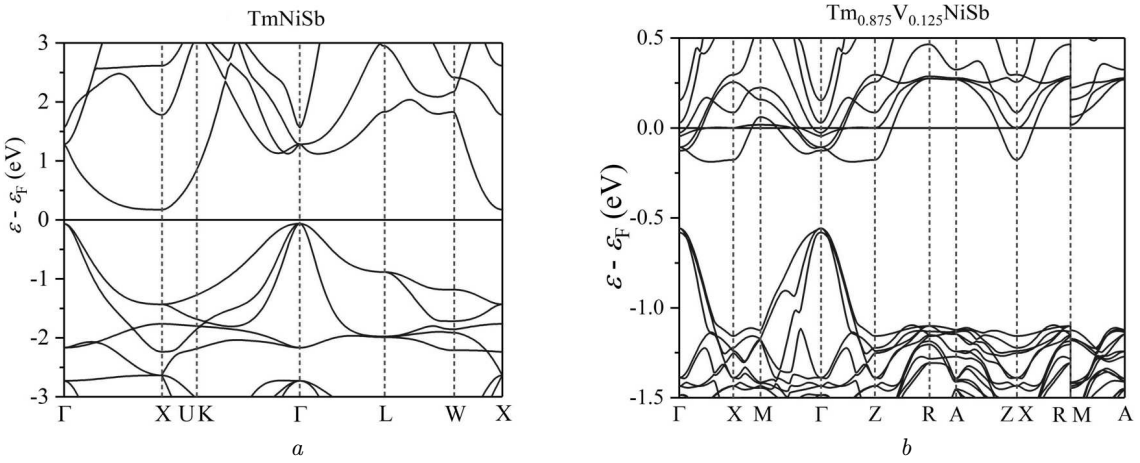

Fig. 6. Band structure (PAW method) of ordered TmNiSb (*a*) and $Tm_{0.875}V_{0.125}NiSb$ (*b*)

of conductivity and, as a result, the change in thermopower coefficient from positive to negative which is expected to occur at $x(V) \approx 0.02$.

3.3. Electrical transport properties

The temperature and concentration dependences of resistivity ρ and thermopower coefficient α of $Tm_{1-x}V_xNiSb$, $0 \le x \le 0.06$, are shown in Figs. 9 and 10. The $\ln(\rho(1/T))$ and $\alpha(1/T)$ dependencies are typical for doped and compensated semiconductors with high- and low-temperature activation regions, which indicates the presence of several mechanisms of electrical conductivity [27]. The $\ln(\rho(1/T))$ dependence is described using the well-known rela-

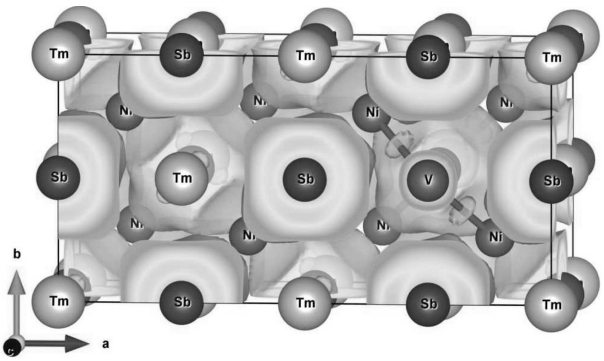

Fig. 7. Isosurface of the electron localization function (ELF = = 0.375) of $Tm_{0.875}V_{0.125}NiSb$ 2×1 × 1 supercell (PAW method)

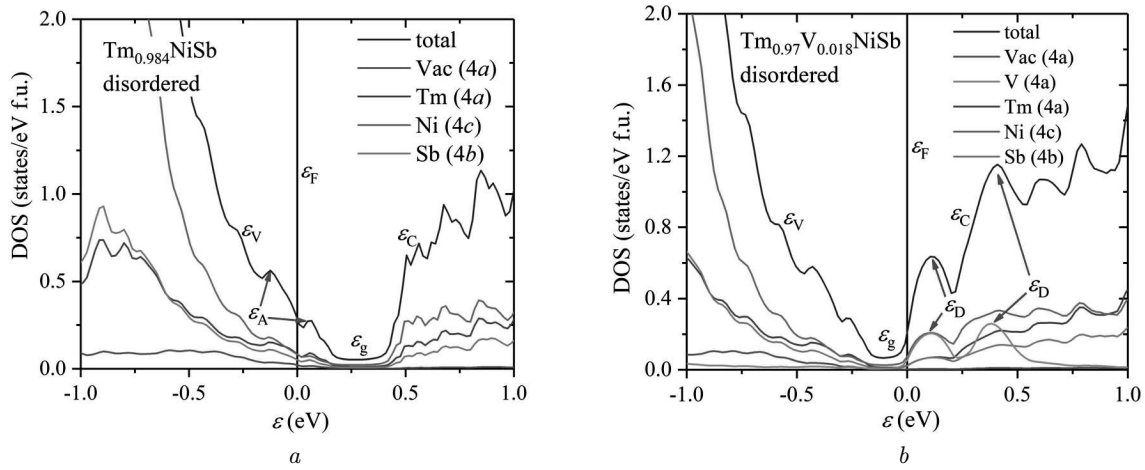

Fig. 8. Distribution of the density of electronic states DOS (KKR-CPA method) of $Tm_{0.984}NiSb$ (a) and $Tm_{0.97}V_{0.018}NiSb$ (b) with disoredered models of their crystal structure. The Fermi level is shifted to 0 eV

tion (1) [27]:

$$\rho^{-1}(T) = \rho_1^{-1} \exp\left(-\frac{\varepsilon_1^\rho}{k_B T}\right) + \rho_3^{-1} \exp\left(-\frac{\varepsilon_3^\rho}{k_B T}\right), \quad (1)$$

where the first term describes the activation of charge carriers ε_1^ρ from the Fermi level ε_F into the continuous band of energies, and the second, low-temperature, hopping conductivity ε_3^ρ with energies close to the Fermi energy ε_F. The temperature dependence of the thermopower coefficient $\alpha(1/T, x)$ (Fig. 10) is described by formula (2) [28]:

$$\alpha = \frac{k_B}{e}\left(\frac{\varepsilon_i^\alpha}{k_B T} - \gamma + 1\right), \quad (2)$$

where γ is a parameter that depends on the nature of scattering mechanisms. According to formula (2), the values of the activation energies ε_1^α and ε_3^α were calculated from the high- and low-temperature activation regions of the thermopower coefficient dependencies $\alpha(1/T, x)$, which are proportional to the modulation amplitudes of the continuous band of energies and small-scale fluctuation, respectively [29]: the higher the degree of compensation, the greater the modulation amplitude of the ε_1^α bands. It turned out that in the p-TmNiSb semiconductor, the Fermi level ε_F lies at a distance of $\varepsilon_1^\rho = 53.4$ meV from the top of the valence band ε_V, and the amplitude of the modulation of the continuous band energies is $\varepsilon_1^\alpha = 70.9$ meV (Fig. 11, a). Note that this result is close to the one obtained earlier in [9].

The change in resistivity $\rho(x, T)$ and thermopower coefficient $\alpha(x, T)$ of $Tm_{1-x}V_xNiSb$, $0 \le x \le 0.06$, is not linear, reflecting complex changes in the crystal and band structures (Fig. 10). Thus, doping p-TmNiSb with the smallest concentration of V atoms available in the experiment leads to a decreasing the resistivity $\rho(x, T)$ in the range $0 \le x \le 0.02$ for all investigated temperatures – for example, at $T = 80$ K from $\rho = 91.1$ $\mu\Omega\times$m ($x = 0$) to $\rho = 67.7$ $\mu\Omega\times$m ($x = 0.02$). At the same time, the thermopower coefficient $\alpha(x, T)$ at these concentrations is positive, indicating the location of the Fermi level ε_F in the band gap ε_g near the valence band ε_V.

This conclusion is also confirmed by the behavior of the Fermi energy ε_F (Fig. 10, a) at the concentration range $0 \le x \le 0.02$, obtained from the temperature dependences $\ln(\rho(1/T))$ (Fig. 9). If in p-TmNiSb the Fermi level ε_F is located at a distance of 53.4 meV from the top of the valence band ε_V, in the doped p-$Tm_{0.98}V_{0.02}NiSb$ it approached the ε_V band at a distance of 32.2 meV. Such a situation is possible in a p-type semiconductor only if the concentration of acceptor states increases. An increase of the acceptor concentration in p-$Tm_{0.98}V_{0.02}NiSb$ is also indicated by the nature of the change in the modulation amplitude of the continuous band of energies $\varepsilon_1^\alpha(x)$ (Fig. 11, a). Thus, if in p-TmNiSb the modulation amplitude of the bands was $\varepsilon_1^\alpha = 70.9$ meV, in p-$Tm_{0.98}V_{0.02}NiSb$ it decreased to 31.1 meV, indicating a decrease of the compensation by a factor of ~2.3 which is possible if additional acceptor states

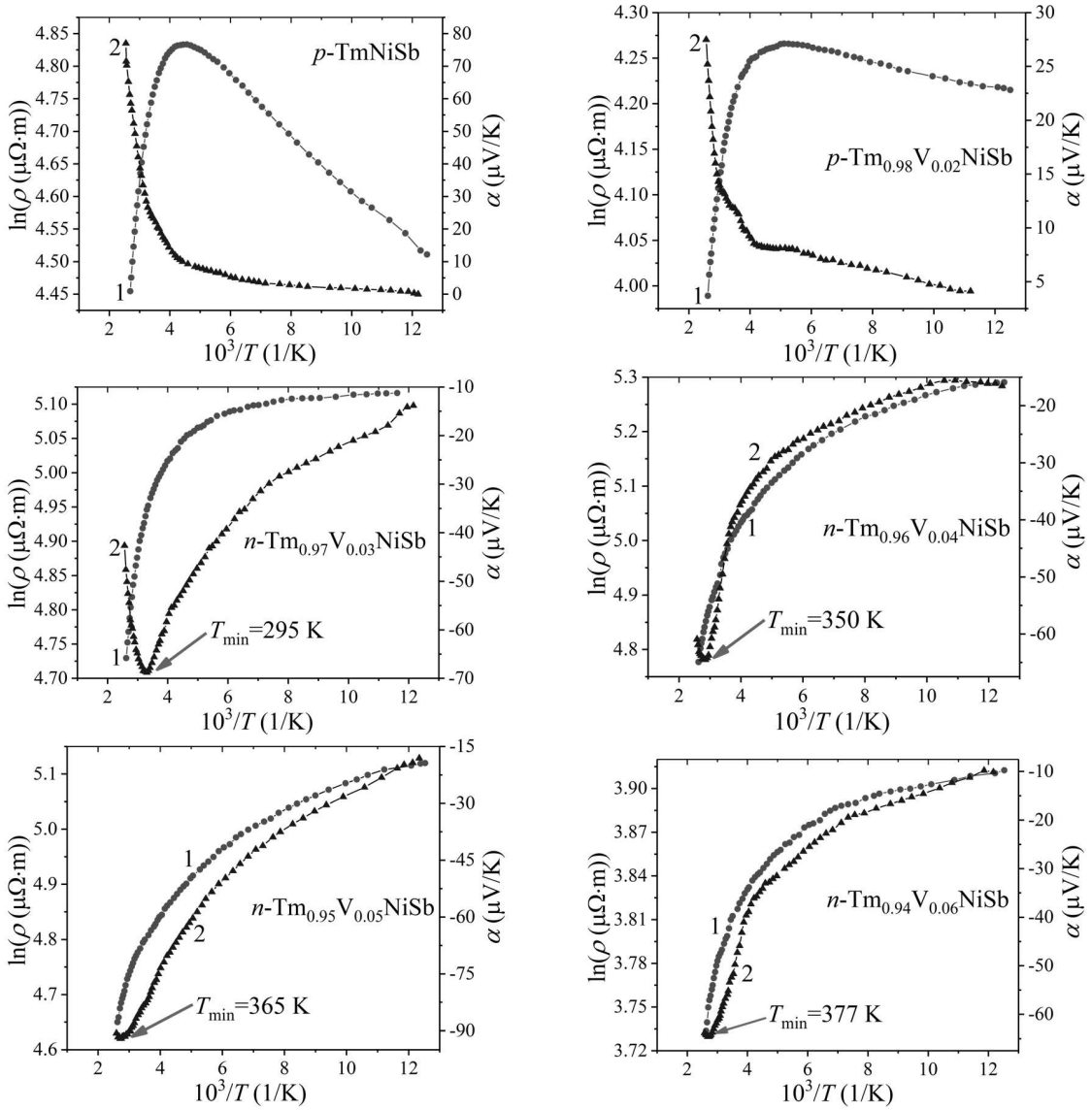

Fig. 9. Temperature dependences of resistivity $\ln(\rho(1/T, x))$ (1) and thermopower coefficient $\alpha(1/T, x)$ (2) of $Tm_{1-x}V_xNiSb$

are generated or the number of donor states is reduced. Since there are no prerequisites for reducing the concentration of donors in p-$Tm_{0.98}V_{0.02}NiSb$, acceptors are generated in the semiconductor. This fact makes it impossible to explain the experimental results solely by replacing Tm atoms with V within the ordered crystal structure model. It requires the disordered structural model of TmNiSb (Fig. 8), in which the crystallographic site 4*a* of Tm atoms contains ∼1.6% vacancies that ensures the *p*-type of conductivity of $Tm_{1-x}V_xNiSb$ in the concentration range $0 \le x \le 0.02$.

At higher concentrations of V atoms ($0.02 < x \le 0.04$), the resistivity $\rho(x, T)$ of $Tm_{1-x}V_xNiSb$ increases, for example, at $T = 80$ K from $\rho = 67.7$ $\mu\Omega\times$m ($x = 0.02$) to $\rho = 200.3$ $\mu\Omega\times$m ($x = 0.04$). At a concentrations $x > 0.02$, there is a change in the sign of the thermopower coefficient $\alpha(x, T)$ from positive to negative, and electrons become the main charge carriers (Fig. 10). This cor-

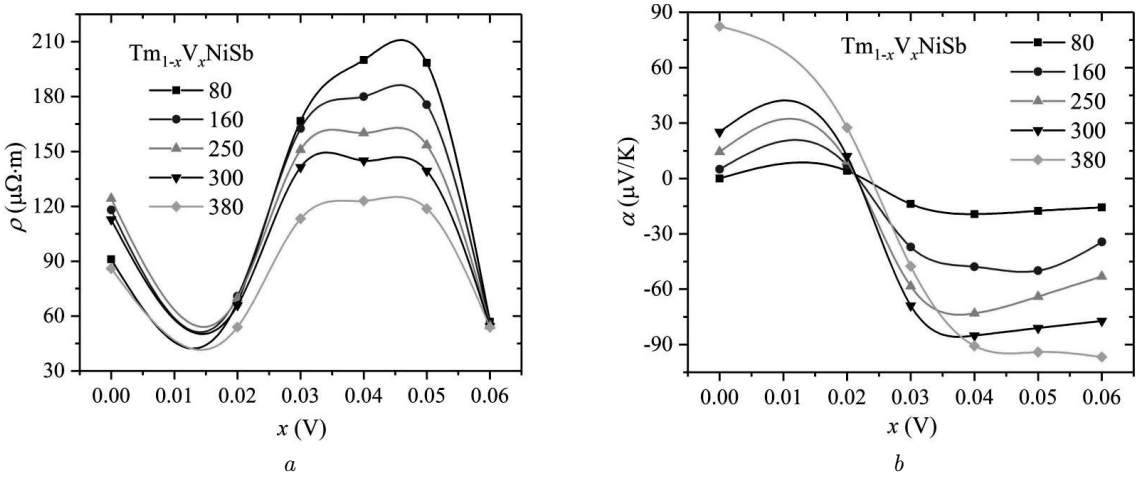

Fig. 10. Variation of the specific resistivity $\rho(x,T)$ (a) and the thermopower coefficient $\alpha(x,T)$ (b) of $Tm_{1-x}V_xNiSb$ at different temperatures

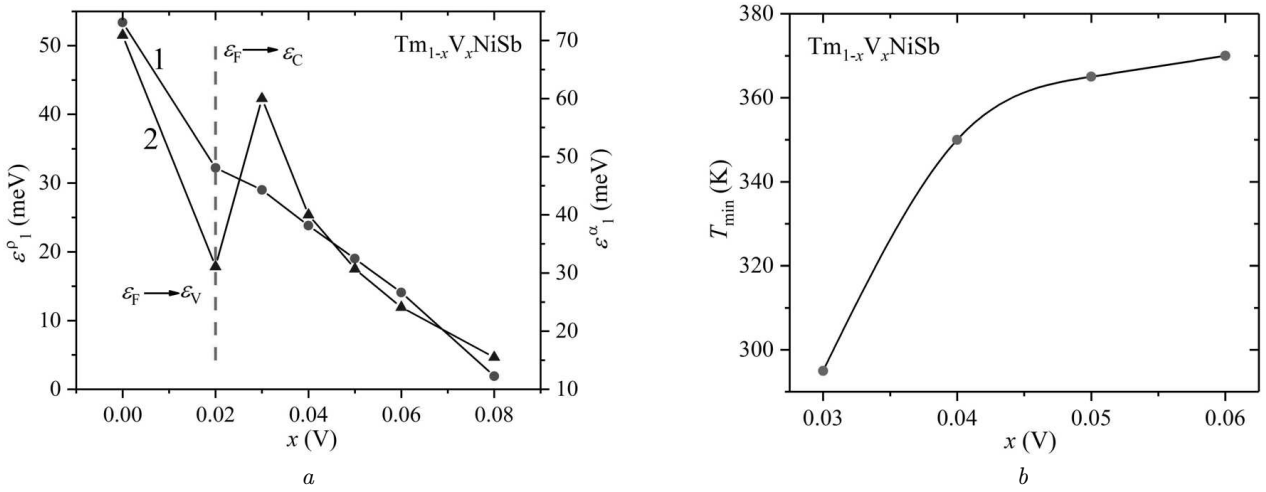

Fig. 11. Change in values of activation energies $\epsilon_1^{\rho}(x)$ (1), $\epsilon_1^{\alpha}(x)$ (2) (a) and a change in temperature values $T_{\min}$ depending on $\alpha(1/T,x)$ (b) of $Tm_{1-x}V_xNiSb$

relates well with Fig. 3, where the number of valence electrons at the $4a$ site reaches $3e$/atom at $x(V) = 0.014$ for the model with disordered crystal structure. The same number of valence electrons at this crystallographic site is expected for the ordered TmNiSb with the Fermi level at the middle of the band gap resulting in a fully compensated semiconductor. An increase in resistivity $\rho(x,T)$ in the range $0.02 < x \leq 0.04$ and a change in the sign of the thermopower coefficient $\alpha(x,T)$ are evidence of the appearance of a source of free electrons in the semiconductor. At the same time, a smaller part of the generated electrons is captured by acceptors presented in the semiconductor, neutralizing them and decreasing the holes' concentration.

The increase in the concentration of donor states in $Tm_{1-x}V_xNiSb$ is accompanied by the almost linear drift of the Fermi level ε_F to the conduction band ε_C (Fig. 11, a). If in $Tm_{0.96}V_{0.04}NiSb$ the Fermi level ε_F was at a distance of 24.1 meV from the conduction band ε_C, already in $Tm_{0.94}V_{0.06}NiSb$ this distance is reduced to 14.1 meV. The modulation amplitude ε_1^{α} in n-$Tm_{0.97}V_{0.03}NiSb$ equals 60.3 meV, which decreases at $x > 0.03$, indicating the predominant generation of donors over acceptors in $Tm_{1-x}V_xNiSb$ (Fig. 11, a). Therefore, the decreased

resistivity $\rho(x,T)$ and the negative thermopower coefficient $\alpha(x,T)$ of $Tm_{1-x}V_xNiSb$ at concentrations $x > 0.04$ (Fig. 9) are due to an increase in the concentration of free electrons.

Despite the sign of the thermopower coefficient $\alpha(1/T,x)$ changes gradually and remains positive at concentrations $0 \le x \le 0.02$, already in $Tm_{0.97}V_{0.03}NiSb$ the sign changes to negative and the dependence $\alpha(1/T,x)$ becomes non-monotonic (Fig. 9). At a temperature of $T_{\min} \approx 295$ K, the dependence passes through a minimum. With increasing temperature, the thermopower coefficient decreases rapidly. A tendency to a possible sign change at higher temperatures, which was not reached in the experiment, is expected. The minimum on $\alpha(1/T,x)$ at $x = 0.03$ and $T_{\min} \approx 295$ K indicates the presence of acceptor states of unknown origin in the n-type semiconductor, whose contribution to conductivity increases with temperature. The thermopower coefficient $\alpha(1/T,x)$ of $Tm_{0.94}V_{0.06}NiSb$ and $Tm_{0.95}V_{0.05}NiSb$ is also characterized by the minima at temperatures $T_{\min} \approx 350$ K and $T_{\min} \approx$ ≈ 365 K, respectively. At a higher concentration of V, such minimum is absent on the $\alpha(1/T,x)$ dependences, and, therefore, the influence of acceptor states on the behavior of the thermopower coefficient at the investigated temperatures was not observed. The concentration dependence of $T_{\min}$ obtained from $\alpha(1/T,x)$ of $Tm_{1-x}V_xNiSb$ (Fig. 11, *b)* reveals that, with the increasing of the V content, the $T_{\min}$ increases. The acceptor states that appear in $Tm_{1-x}V_xNiSb$ at high temperatures have a different depths and origins than the acceptor states caused by vacancies at the 4*a* position of Tm atoms. These additional acceptor states may originate from the vacancies at the Ni 4*c* site, which increases with temperature and is reflected in the formation of the homogeneity region $TmNi_{1-x}Sb$ typical of other RNiSb half-Heusler phases.

4. Conclusions

The results of structural, thermodynamic, electrical transport, and DFT studies of the $Tm_{1-x}V_xNiSb$ solid solution revealed a complex nature of changes in the crystal and electronic structures. The disordered model of the crystal structure of TmNiSb, which contains vacancies at the Tm 4*a* site, explains its p-type conductivity. With the V for Tm substitution, the vacancies and Tm atoms at the 4*a* site are simultaneously filled with V in different ratios up to $x(V) = 0.03$, causing an increase in the lattice volume. When all vacancies are filled at higher concentrations of vanadium, the average atomic radius at the 4*a* site starts to decrease, inducing a decrease in the unit cell parameter a. The mechanism of the formation of two types of acceptor states with different depths of occurrence is experimentally determined: small acceptors generated by vacancies in the p-TmNiSb structure and deep ones presumably formed by the vacancies at the Ni 4*c* site and corresponding to the homogeneity region $TmNi_{1-x}Sb$ typical of other RNiSb half-Heusler phases. The concentration ratio of the generated defects determines the position of the Fermi level ε_F and the conductivity mechanisms. The results of DFT modeling, including the ground-state energy, distribution of the density of electronic states (DOS), and the band structure of $Tm_{1-x}V_xNiSb$, are consistent with experimental results.

The authors thank U. Nitzsche for technical assistance in running DFT calculations on the ITF/IFW cluster. We would like to acknowledge the financial support from the Ministry of Education and Science of Ukraine under Grants No. 0124U000989, No. 0124U001146. Authors Yu. Stadnyk, L. Romaka, A. Horyn, Yu. Demchenko also thank the Simons Foundation (Award Number: 1290588) for financial support. V.V.R is funded by the DFG (project-id 463049368).

1. V.A. Romaka, Yu.V. Stadnyk, V.Ya. Krayovskyy, L.P. Romaka, O.P. Guk, V.V. Romaka, M.M. Mykyychuk, A.M. Horyn. *The Latest Heat-Sensitive Materials and Temperature Transducers* (Lviv Polytechnic Publishing House, 2020).
2. J. Bos, R. Downie. Half-Heusler thermoelectrics: A complex class of materials. *Phys.: Condens. Matter.* **26**, 433201 (2014).
3. L. Huang, Q. Zhang, Bo Yuan, X. Lai, X. Yan, Z. Ren. Recent progress in half-Heusler thermoelectric materials. *Mater. Res. Bull.* **76**, 107 (2016).
4. K. Xia, C. Hu, C. Fu, X. Zhao, T. Zhu. Half-Heusler thermoelectric materials. *Appl. Phys. Lett.* **118**, 140503 (2021).
5. K. Hartjes, W. Jeitschko. Crystal structure and magnetic properties of the lanthanoid nickel antimonides LnNiSb (Ln=La–Nd, Sm, Gd–Tm, Lu). *J. Alloys Compd.* **226**, 81 (1995).
6. I. Karla, J. Pierre, R.V. Skolozdra. Physical properties and giant magnetoresistance in RNiSb compounds. *J. Alloys Compd.* **265**, 42 (1998).

7. R.V. Skolozdra, A. Guzik, A.M. Goryn, J. Pierre. Magnetic and transport properties of RNiSb compounds. *Acta Phys. Polonica* A. **92**,343 (1997).
8. V.V. Romaka, L. Romaka, A. Horyn, P. Rogl, Yu. Stadnyk, N. Melnychenko, M. Orlovskyy, V. Krayovskyy. Peculiarities of thermoelectric half-Heusler phase formation in Gd–Ni–Sb and Lu–Ni–Sb ternary systems. *J. Solid State Chem.* **239**, 145 (2016).
9. V.V. Romaka, L. Romaka, A. Horyn, Yu. Stadnyk. Experimental and theoretical investigation of the Y–Ni–Sb and Tm–Ni–Sb systems. *J. Alloys Compd.* **855**, 157334 (2021).
10. V.V. Romaka, V.A. Romaka, Yu.V. Stadnyk, L.P. Romaka, Y.O. Plevachuk, V.Z. Pashkevich, P.I. Haraniuk, A.M. Horyn. Features of the generation of the energy states in the semiconductor $Lu_{1-x}V_xNiSb$. *Ukr. J. Phys.* **68**(4), 274 (2023).
11. V.A. Romaka, Yu. Stadnyk, L. Romaka, A. Horyn, V. Pashkevich, H. Nychyporuk, P. Garanyuk. Investigation of thermoelectric material based on $Lu_{1-x}Zr_xNiSb$ solid solution. I. Experimental results. *J. Phys. and Chem. Sol. State.* **23**, 235–241 (2022).
12. V.A. Romaka, Yu. Stadnyk, L. Romaka, V.V. Romaka, P. Demchenko, V. Pashkevich, A. Horyn. Investigation of thermoelectric material based on $Lu_{1-x}Zr_xNiSb$ solid solution. II. Modeling of characteristics. *J. Phys. and Chem. Sol. State.* **23**, 4974 (2022).
13. V.A. Romaka, Yu. Stadnyk, L. Romaka, V. Krayovskyy, A. Horyn, P. Klyzub, V. Pashkevych. Study of the structural, electrokinetic and magnetic characteristics of the $Er_{1-x}Zr_xNiSb$ semiconductor. *J. Phys. and Chem. Sol. State.* **21**, 689 (2020).
14. V.V. Romaka, V.A. Romaka, Yu.V. Stadnyk, L.P. Romaka, P.Y. Demchenko, V.Z. Pashkevych, A.M. Horyn. Featutes of mechanisms of electrical conductivity in semiconductive solid solution $Lu_{1-x}Sc_xNiSb$. *Ukr. J. Phys.* **67**, 370 (2022).
15. Yu. Stadnyk, V.A. Romaka, A. Horyn, V.V. Romaka, L. Romaka, P. Klyzub, V. Pashkevich, A. Gorpenyuk. Modeling of structural and energetic parameters of p-$Er_{1-x}Sc_xNiSb$ semiconductor. *J. Phys. and Chem. Sol. State.* **22**, 509 (2021).
16. I. Wolanska, K. Synoradzki, K. Ciesielski, K. Zaleski, P. Skokowski, D. Kaczorowski. Enhanced thermoelectric power factor of half-Heusler solid solution $Sc_{1-x}Tm_xNiSb$ prepared by high-pressure high-temperature sintering method. *Mater. Chem. Phys.* **227**, 29 (2019).
17. T. Roisnel, J. Rodriguez-Carvajal. WinPLOTR: a windows tool for powder diffraction patterns analysis. *Mater. Sci. Forum, Proc. EPDIC7.* **378–381**, 118 (2001).
18. G. Kresse, J. Hafner. Ab initio molecular dynamics for liquid metals. *Phys. Rev. B* **47**, 558 (1993).
19. G. Kresse, D. Joubert. From ultrasoft pseudopotentials to the projector augmented-wave method. *Phys. Rev. B* **59**, 1758 (1999).
20. J.P. Perdew, K. Burke, M. Ernzerhof. Generalized gradient approximation made simple. *Phys. Rev. Lett.* **77** (18), 3865 (1996).
21. H.J. Monkhorst, J.K. Pack. Special points for Brillouin-zone integrations. *Phys. Rev. B* **13**, 5188 (1976).
22. K. Okhotnikov, T. Charpentier, S. Cadars. Supercell program: a combinatorial structure-generation approach for the local-level modeling of atomic substitutions and partial occupancies in crystals. *J. Cheminform.* **8** (17), 1 (2016).
23. P. Vinet, J.H. Rose, J.S. Jr Ferrante. Universal features of the equation of state of solids. *J. Phys.: Codens. Matter.* **1**, 1941 (1989).
24. H. Akai. Fast Korringa–Kohn–Rostoker coherent potential approximation and its application to FCC Ni-Fe systems. *J. Phys.: Condens. Matter.* **1**, 8045 (1989).
25. V.L. Moruzzi, J.F. Janak, A.R. Williams. *Calculated Electronic Properties of Metals* (Pergamon Press, 1978).
26. V.V. Romaka, G. Rogl, A. Grytsiv, P. Rogl. Determination of structural disorder in Heusler-type phases. *Comput. Mater. Sci.* **172**, 109307 (2020).
27. B.I. Shklovskii, A.L. Efros. *Electronic Properties of Doped Semiconductors* (Springer Verlag, 1984).
28. N.F. Mott, E.A. Davis. *Electron Processes in Non-Crystalline Materials* (Clarendon Press, 1979).
29. V.A. Romaka, E.K. Hlil, Ya.V. Skolozdra, P. Rogl, Yu.V. Stadnyk, L.P. Romaka, A.M. Goryn. Features of the mechanisms of generation and "Healing" of structural defects in the heavily doped intermetallic semiconductor *n*-ZrNiSn. *Semiconductors.* **43**, 1115 (2009).

Received 28.05.24

В.В. Ромака, В.А. Ромака,
Ю.В. Стадник, Л.П. Ромака, А.М. Горинь,
П.Ю. Демченко, В.З. Пашкевич

МЕХАНІЗМИ ЕЛЕКТРОПРОВІДНОСТІ У НАПІВПРОВІДНИКУ $Tm_{1-x}V_xNiSb$

Досліджено структурні, термодинамічні, кінетичні та енергетичні властивості напівпровідників $Tm_{1-x}V_xNiSb$ з $0 \leq x \leq 0{,}10$ в інтервалі температур $T = 80$–400 K. Проведене дослідження показує, що кристалічна структура TmNiSb ($x = 0$) є невпорядкованою і містить до 2% вакансій у кристалографічній позиції $4a$ атомів Tm, які з ростом x до $x = 0{,}03$ поступово заповнюються атомами V; подальше збільшення x супроводжується заміщенням атомів Tm атомами V. Експериментально встановлено механізм формування двох сортів акцепторних станів з різною глибиною залягання: мілких акцепторів, породжених вакансіями у структурі *p*-TmNiSb, та глибоких акцепторів, утворених вакансіями у кристалографічній позиції $4c$ атомів Ni, які відповідають області гомогенності сполуки $Tm_xNi_{1-x}Sb$, типовій для інших фаз *R*NiSb. Результати моделювання в рамках теорії функціонала густини, включно із енергією основного стану, розподілом густини електронних станів і зонною структурою $Tm_{1-x}V_xNiSb$, узгоджуються з результатами експериментальних досліджень.

Ключові слова: напівгойслерівські фази, рівень Фермі, електронна структура, електроопір, коефіцієнт термоелектрорушійної сили.